Observation of Single Colloidal Platinum Nanocrystal Growth Trajectories

Haimei Zheng *et al.*

Science **324**, 1309 (2009);
DOI: 10.1126/science.1172104

beam current; 30-s counting time; and Al-Kα, Cu-Kα, and Fe-Kα lines.
13. L. Zhang, R. Lück, *Z. Metallkd.* **94**, 774 (2003).
14. The instrument was an Oxford Diffraction Excalibur PX Ultra diffractometer with a 165-mm diagonal Onyx charge-coupled device detector at 2.5:1 demagnification. The program *Crysalis* RED (Oxford Diffraction 2006) was used to convert the observed diffraction rings into a conventional XRD pattern.
15. T. C. Lubensky, J. E. S. Socolar, P. J. Steinhardt, P. A. Bancel, P. A. Heiney, *Phys. Rev. Lett.* **57**, 1440 (1986).
16. The instrument was a Philips CM200-FEG TEM configured with a super-twin lens. The instrument was operated at 200 kV with a vacuum pressure of ~2×10^{-7} torr; the electron beam size ranged from 50 nm to 0.3 μm.
17. D. Levine, T. C. Lubensky, S. Ostlund, S. Ramaswamy, P. J. Steinhardt, J. Toner, *Phys. Rev. Lett.* **54**, 1520 (1985).
18. B. Dam, A. Janner, J. D. H. Donnay, *Phys. Rev. Lett.* **55**, 2301 (1985).
19. E. Makovicky, B. G. Hyde, *Struct. Bonding* **46**, 101 (1981).
20. We are indebted to L. Hollister and G. MacPherson for their critical examination of the results, especially regarding the issue of natural origin. We also thank P. Bonazzi, K. Deffeyes, S. Menchetti, and P. Spry for useful discussions and S. Bambi at the Museo di Storia Naturale for the photograph of the original sample in Fig. 1A. L.B. thanks the Ministerio dell'Istruzione dell'Università e della Ricerca Programma di Ricerca Nazionale 2007 project "Complexity in minerals: modulation, phase transition, structural disorder," issued to S. Menchetti. This work was supported in part by U.S. Department of Energy grant DE-FG02-91ER40671 (P.J.S.), the NSF MRSEC program through New York University (grant DMR-0820341; P.J.S.), the Princeton Center for Complex Materials (grant DMR-0819860; N.Y.), and the New Jersey Commission of Science and Technology (N.Y.).

12 January 2009; accepted 23 March 2009
10.1126/science.1170827

Observation of Single Colloidal Platinum Nanocrystal Growth Trajectories

Haimei Zheng,[1,2,3] Rachel K. Smith,[3]* Young-wook Jun,[2,3]* Christian Kisielowski,[1,2] Ulrich Dahmen,[1,2]† A. Paul Alivisatos[2,3]†

Understanding of colloidal nanocrystal growth mechanisms is essential for the syntheses of nanocrystals with desired physical properties. The classical model for the growth of monodisperse nanocrystals assumes a discrete nucleation stage followed by growth via monomer attachment, but has overlooked particle-particle interactions. Recent studies have suggested that interactions between particles play an important role. Using in situ transmission electron microscopy, we show that platinum nanocrystals can grow either by monomer attachment from solution or by particle coalescence. Through the combination of these two processes, an initially broad size distribution can spontaneously narrow into a nearly monodisperse distribution. We suggest that colloidal nanocrystals take different pathways of growth based on their size- and morphology-dependent internal energies.

The growth of colloidal nanocrystals has advanced remarkably, and now it is possible to make colloidal nanocrystals of a wide range of solids, ranging from metals to semiconductors and insulators, with narrow size distributions (variations in diameter less than 5%) and high crystallinity (*1*–*5*). It is also possible to control their shapes, from spheres to disks or rods, as well as their topology (solid, hollow, nested) and their connectivity and branching patterns by adjusting the growth parameters, such as surfactant, concentration, or temperature (*6*–*11*). The current state of nanocrystal synthesis has been largely achieved empirically with some classical models (*12*–*14*) for particle growth serving as guides. Here, we demonstrate that it is possible to directly observe the growth trajectories of individual colloidal nanocrystals in solution by using a liquid cell that operates inside a transmission electron microscope (TEM), and that these trajectories reveal a set of pathways more complex than those previously envisioned.

Consider the simplest case of a narrow size distribution of nearly spherical colloidal nanoparticles. A model based on kinetics that can account for this size distribution was proposed by LaMer and Dinegar (*12*) and improved by Reiss (*13*). An abrupt increase in monomer concentration induces a burst of nucleation events followed by a period of rapid growth. The initial broad size distribution because of a spread in nucleation time or other variations such as mixing can be corrected with "size distribution focusing," in which small crystals "catch up" with larger ones because the growth rate of nanocrystals decreases as the size increases (*1*). Inhibition of particle aggregation is typically achieved by using surfactant ligands that stabilize the particle surface and provide a barrier to coalescence. The thinking underlying this approach has guided many syntheses (*1*, *2*, *4*). A second scenario for nanocrystal control employs an equilibrium approach. One devises a system in which the binding of surfactant to the nanoparticle surface is nearly as strong as the bonds within the crystal, strong enough then to thermodynamically drive the system toward a particular average size for a given concentration of surfactant and monomeric species (*15*–*17*). These two distinct models consider only the possibility of particle growth through the addition of monomeric species. However, there is substantial evidence that particle coalescence or even oriented attachment can also play a role in nanocrystal growth (*18*–*22*). The lack of consensus on the controlling mechanisms is mainly due to the lack of direct evidence for nanocrystal growth in solution. In situ observation of the dynamic growth process is expected to substantially advance our understanding of nanocrystal growth mechanisms,

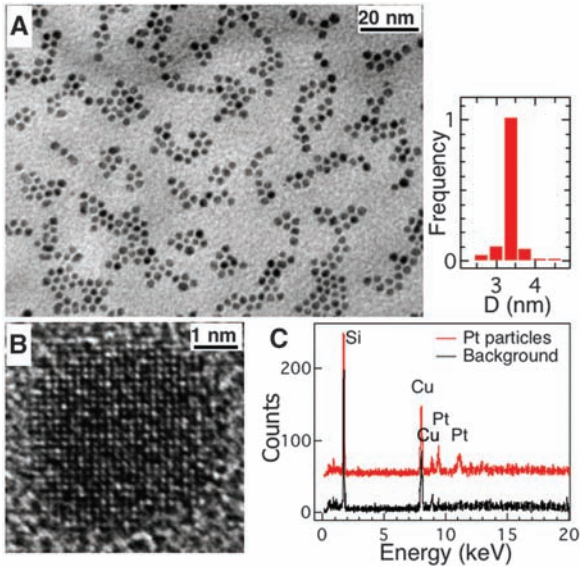

Fig. 1. TEM of Pt nanocrystals synthesized in a liquid cell. (**A**) Bright-field TEM image of Pt nanocrystals with a histogram of particle size distribution, obtained from measurements of 150 particles. (**B**) High-resolution TEM image of a Pt nanocrystal, which was recorded after the in situ experiment. (**C**) EDS spectra from Pt nanocrystals (red) and background (black) obtained ex situ from the same liquid cell. The observed Si and Cu signals are from the silicon nitride membrane window and the cover of the liquid cell, respectively.

[1]National Center for Electron Microcopy, Lawrence Berkeley National Laboratory, Berkeley, CA 94720, USA. [2]Materials Sciences Division, Lawrence Berkeley National Laboratory, Berkeley, CA 94720, USA. [3]Department of Chemistry, University of California, Berkeley, CA 94720, USA.

*These authors contributed equally to this paper.
†To whom correspondence should be addressed. E-mail: udahmen@lbl.gov (U.D.); alivis@berkeley.edu (A.P.A.)

although its application to specific syntheses will have to take into account factors such as the thermodynamic and geometric differences between microscopic in situ and macroscopic flask experiments.

In order to observe colloidal nanocrystal growth, one needs a technique that can image through liquids during the chemical reaction with nanometer resolution and in real time. Williams *et al.* have developed a liquid cell reactor that can be placed in a special TEM sample holder, which was used to image the dynamic growth of Cu clusters on a surface during electrochemical plating by using a TEM with a resolution of 5 nm (*23*) [see also other related techniques in (*24*–*26*)].We employed this TEM capability in a self-contained liquid cell with an improved resolution in the subnanometer range (fig. S1) (*27*). We used these disposable liquid cells to image platinum nanocrystal growth in solution in situ using a JEOL3010 microscope operated at 300 kV. Because the cells fit into a standard TEM sample holder, we also used CM300 and CM200 TEMs equipped with an x-ray detector for high-resolution TEM imaging and elemental analysis ex situ on the same cell. We prepared a stock solution for synthesis by dissolving $Pt(acetylacetonate)_2$ (10 mg/mL) in a mixture of *o*-dichlorobenzene and oleylamine (9:1 in volume ratio). We loaded about 100 nanoliters of the growth solution into the reservoir of a liquid cell, and the solution was drawn into the cell by capillary force. Subsequently, the cell was sealed and loaded into the microscope. Within the electron-transparent window, the reaction solution of about 200 nm in thickness was confined between two silicon nitride membranes (25 nm each).

A key feature of these experiments is the ability to use the electron beam to induce the nucleation of Pt nanocrystals. The growth of Pt nanocrystals in solution was initiated by the electron beam irradiation, and a constant beam intensity of 2×10^4 to 14×10^4 A/m^2 was maintained during the growth (*27*). The beam intensity varied briefly in the initial exposure to the electron beam (a few seconds) during the time required to focus for imaging. Nanocrystals nucleated and grew during this period of time. Under constant illumination, there was normally a subsequent round of nucleation followed by growth (movie S1; also see movie S2 for comparison). Figure 1A shows platinum nanocrystals obtained inside a liquid cell by the exposure of the growth solution to the electron beam for about 5 min. Nearly monodisperse nanoparticles with an average diameter of 3.4 nm and a SD of 8% were obtained (Fig. 1A, inset). The platinum nanoparticles were mostly single crystalline with a face-centered cubic structure (Fig. 1B) and a composition of pure Pt, as confirmed by energy-dispersive x-ray spectroscopy (EDS) (Fig. 1C).

In situ observation of the Pt nanoparticle growth provides details of the growth kinetics. Figure 2 shows a sequence of video images recorded at 0.0 s, 12.1 s, 24.2 s, and 77.0 s of exposure to electron beam radiation (movie S1). From the initial growth solution of Pt^{2+} precursor, a large number of Pt nanocrystals emerged, and new particles continued to appear. The nucleation under a constant electron beam irradiation spanned more than 10 s (see the number of particles as a function of time in Fig. 2B). Particle growth and nucleation occurred in parallel (see particles highlighted by arrows in Fig. 2A, indicating examples of growth). Along with the conventional particle growth by means of monomer addition from solution, frequent coalescence events between the particles were observed. At the early stage of the growth, the number of particles gradually increased and reached a maximum at 21.0 s. Subsequently, the number of particles dropped significantly and eventually settled at a constant value. Although some smaller particles were seen to dissolve completely, the decrease in the number of particles was mainly due to the coalescence events between individual particles (see the number of coalescence events as a function of time in Fig. 2B).

We examined the particles that have similar initial sizes but grow along different pathways. Figure 3A shows a sequence of video frames of two particles that were taken from the same field of view (fig. S2). The particle formed by means of simple growth shows a continuous increase of size and maintains a nearly spherical shape. In addition, mostly uniform diffraction contrast within the particle was observed, indicating single crystalline characteristics throughout the growth. However, the coalesced particle shows both shape changes and different diffraction contrast, indicating polycrystalline characteristics within the particle after the coalescence event. Eventually (about 16.0 s after the coalescence event) it forms a single crystalline particle with a nearly spherical shape. This is characteristic of punctuated growth, in which the growth of the coalesced particles pauses after coalescence during the period of structural relaxation. These pauses contribute to the situation in

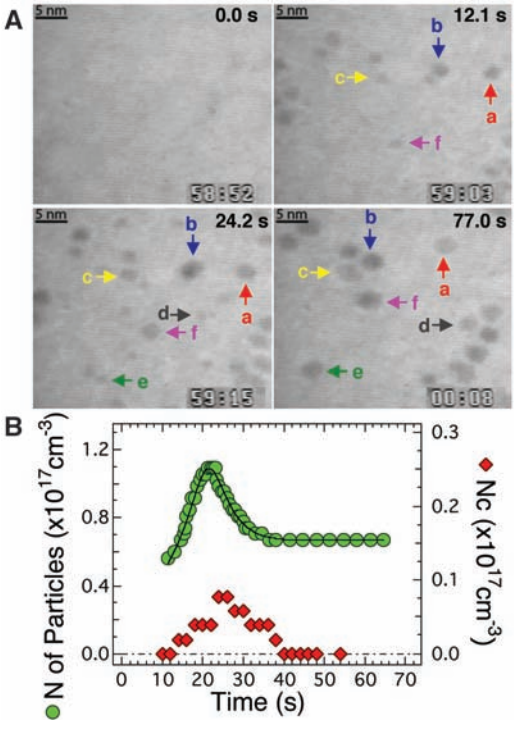

Fig. 2. Growth and coalescence of Pt nanocrystals. (**A**) Video images acquired at 0.0 s, 12.1 s, 24.2 s, and 77.0 s of exposure to the electron beam. Specific particles are labeled with arrows. The growth trajectories of these individual particles reveal the multiple pathways leading to size focusing. (**B**) Number of particles (left axis) and number of coalescence events (Nc, right axis) during an interval of 2.0 s versus time. Particles nucleate and grow during the adjustment of focus for imaging (0 to 10 s), the details of which were not available.

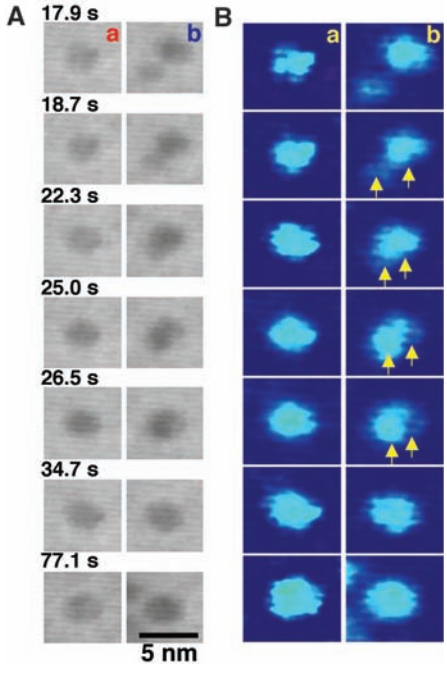

Fig. 3. Comparison of different growth trajectories. (**A**) Video images showing simple growth by means of monomer addition (left column) or growth by means of coalescence (right column). Particles are selected from the same field of view. (**B**) Enlarged (1.5 times) color images of (A). Distinct contrast changes are highlighted with arrows indicating recrystallization, which were observed in the coalesced particle but not in the case of simple growth.

which particles that are formed by the steady simple growth process in order to "catch up" so that the two types of particles show similar final sizes.

We considered the evolution of particle size distribution in light of the observed single-particle growth trajectories. Figure 4A shows the histograms of particle size distribution at different stages of growth (19.7 s, 24.2 s, 30.3 s, and 77.0 s; for each plot, we measured about 120 to 170 particles within an area of 50 nm by 60 nm and in intervals of 100 ms). At the early stages, particle size distributions are broad, because of the spread of nucleation events over time. At 24.2 s, we observed a bimodal distribution. At a later stage, the distribution has a single peak, and the initially broad distribution has spontaneously narrowed.

In order to understand this size-focusing behavior, we have examined the growth trajectories of each individual nanoparticle. Figure 4B shows particle size as a function of growth time for a few selected particles as examples (particles are highlighted by arrows in Fig. 2A), in which an effective size of $d = 2 \times \sqrt{A/\pi}$ was used, where A is the projected area of the particle in the video images. A particle evolving by means of simple growth shows a continuous increase of size until it reaches a saturation stage (particle a). However, particles resulting from coalescence events (particles b to e) show a jump of particle size after each coalescence event. A smaller particle can "catch up" to the size of a bigger particle through multiple coalescence events. The fact that multiple coalescence events are more commonly observed among the small particles is attributed to their higher energy due to a larger surface-to-volume ratio and an increased collision frequency resulting from a greater mobility. Such growth kinetics of individual nanoparticles deviates from the ensemble behavior, shown in Fig. 4C, which reflects the average particle size within an area of 50 nm by 60 nm as a function of time. The evolution of the mean particle size versus time resembles the trend predicted by classical growth models of a diffusion-controlled Ostwald ripening process (*2*) [the size of the particles (d) is proportional to growth time (t), $d^3 \sim t$]. This illustrates that direct observations of single-particle growth trajectories provide important insights into nanocrystal growth mechanisms, which are not accessible with a conventional analysis on the basis of the ensemble. For example, we found that there is a period of time after a coalescence event during which the coalesced particles cease to grow. After this relaxation period, the particle resumes growth through monomer addition. The combined effects of monomer addition, coalescence, and punctuated growth all contribute to the focusing of the size distribution.

During coalescence, the combined particle has a higher internal energy and chemical potential because of the appearance of grain boundaries and a higher surface energy per volume that is determined by its shape as compared with that of a spherical particle of the same size. Such higher-energy particles may lose monomers (dissolve) in the solution and/or change shape. Similar effects have been observed in the growth of Ge islands from a vapor phase (*28*). In our case, the combined nanoparticle changes shape, forming a spherical particle along with the recrystallization. During this relaxation period, there is a slight decrease of particle size. However, nanocrystals that evolve by means of simple growth show a continuous increase of particle size until reaching a saturation stage (Fig. 4B). We further found that the relaxation time (τ, highlighted in Fig. 4B, inset) increases with the particle size (d) following a power law relationship, $\tau \sim d^{3.3}$ (Fig. 4D). When considering the relaxation process as a recrystallization process in which monomeric species migrate on the two-dimensional nanocrystal surface, such a result is fairly reasonable. The relaxation time is proportional to the total surface area ($A = \frac{1}{4}\pi \times d^2$) and inversely proportional to the mobility (β) of monomers on the particle surface, $\beta \propto \frac{1}{d}$, where $1/d$ is the curvature of the particle. Therefore, the relationship between the relaxation time and the size of the coalesced particles is estimated by $\tau \sim d^3$, which is close to our experimentally observed value. However, this is only a rough estimate. Additional factors, such as variations in the nature of coalescence (oriented or random attachment) or details of size and shape of the coalesced particle need to be considered for more accurate evaluation (*29*).

Additionally, we found that oleylamine surfactants play a large role in the growth of monodisperse platinum nanocrystals. When the amount of oleylamine in the growth solution was decreased (0 to 3%), platinum crystal foils and dendrites were observed (fig. S3).

In summary, we have observed the dynamic growth of colloidal platinum nanocrystals in solution with subnanometer resolution by using a TEM. The evolution of monodisperse platinum nanocrystals involves complex growth trajectories, such as punctuated growth correlated with coalescence events, features that have not been considered in the classical models for nanocrystal growth. Considering coalescence as an alternative to simple growth by attachment of monomeric species, we expect that growth by particle attachment may also play an important role in the synthesis of nanocrystals with more complex shapes. More generally, we have shown that in situ TEM enables the visualization of single nanoparticles in solution with subnanometer resolution and offers great potential for addressing many fundamental issues in materials science, chemistry, and other fields of science.

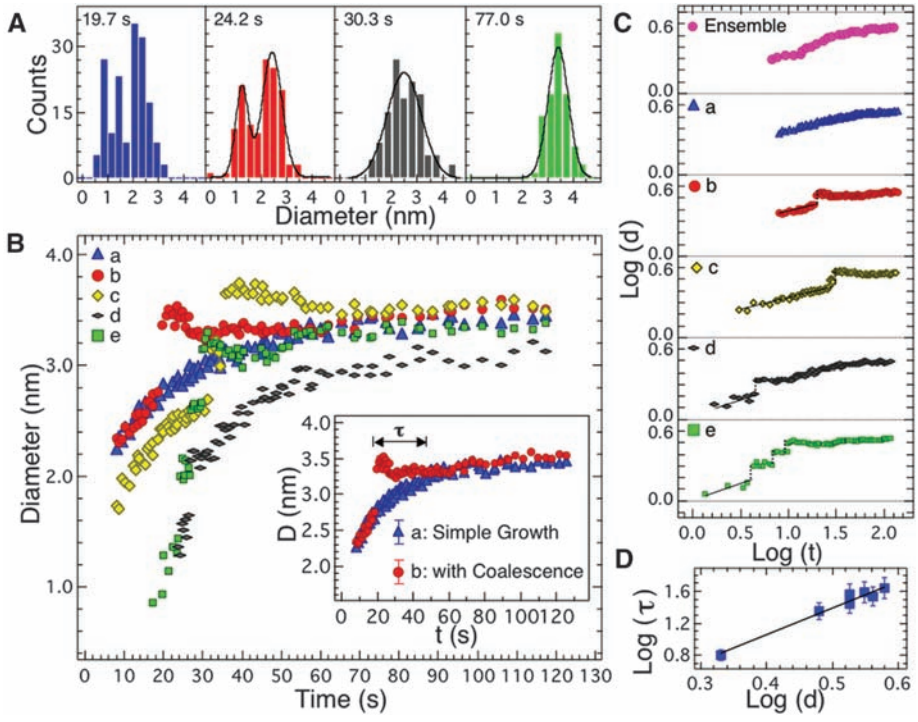

Fig. 4. Growth kinetics of Pt nanoparticles. (**A**) Histograms of particle size distribution at 19.7 s, 24.2 s, 30.3 s, and 77.0 s. Black curves are Gaussian fits. (**B**) Particle size versus growth time. These particles are highlighted in Fig. 2A. Inset shows two types of growth trajectories. A relaxation time (τ) was observed after a coalescence event. Error bars for particle diameter measurements are less than ±0.18 nm. (**C**) Logarithmic relationship of particle size versus growth time for the ensemble and those individual particles in (B). Black lines are guides for the eye, and dashed lines show the coalescence events. (**D**) Logarithmic relationship of relaxation time versus the size of the coalesced particles. Black line shows linear fit.

References and Notes

1. X. G. Peng, J. Wickham, A. P. Alivisatos, *J. Am. Chem. Soc.* **120**, 5343 (1998).
2. C. B. Murray, C. R. Kagan, M. G. Bawendi, *Annu. Rev. Mater. Sci.* **30**, 545 (2000).

3. B. L. Cushing, V. L. Kolesnichenko, C. J. O'Connor, *Chem. Rev.* **104**, 3893 (2004).
4. Y. Yin, A. P. Alivisatos, *Nature* **437**, 664 (2005).
5. D. J. Norris, A. L. Efros, S. C. Erwin, *Science* **319**, 1776 (2008).
6. X. G. Peng *et al*., *Nature* **404**, 59 (2000).
7. L. Manna, E. C. Scher, A. P. Alivisatos, *J. Am. Chem. Soc.* **122**, 12700 (2000).
8. V. F. Puntes, K. M. Krishnan, A. P. Alivisatos, *Science* **291**, 2115 (2001).
9. V. F. Puntes, D. Zanchet, C. K. Erdonmez, A. P. Alivisatos, *J. Am. Chem. Soc.* **124**, 12874 (2002).
10. D. J. Milliron *et al*., *Nature* **430**, 190 (2004).
11. Y. D. Yin *et al*., *Science* **304**, 711 (2004).
12. V. K. LaMer, R. H. Dinergar, *J. Am. Chem. Soc.* **72**, 4847 (1950).
13. H. Reiss, *J. Chem. Phys.* **19**, 482 (1951).
14. T. Sugimoto, *Adv. Colloid Interface Sci.* **28**, 65 (1987).
15. D. V. Leff, P. C. Ohara, J. R. Heath, W. M. Gelbart, *J. Phys. Chem. B* **99**, 7036 (1995).
16. Y. Chen, E. Johnson, X. Peng, *J. Am. Chem. Soc.* **129**, 10937 (2007).
17. Y. A. Yang, H. M. Wu, K. R. Williams, Y. C. Cao, *Angew. Chem. Int. Ed.* **44**, 6712 (2005).
18. J. F. Banfield, S. A. Welch, H. Z. Zhang, T. T. Ebert, R. L. Penn, *Science* **289**, 751 (2000).
19. C. Pacholski, A. Kornowski, H. Weller, *Angew. Chem. Int. Ed.* **41**, 1188 (2002).
20. J. H. Yu *et al*., *J. Am. Chem. Soc.* **127**, 5662 (2005).
21. M. Niederberger, H. Colfen, *Phys. Chem. Chem. Phys.* **8**, 3271 (2006).
22. M. A. Watzky, E. E. Finney, R. G. Finke, *J. Am. Chem. Soc.* **130**, 11959 (2008).
23. M. J. Williamson, R. M. Tromp, P. M. Vereecken, R. Hull, F. M. Ross, *Nat. Mater.* **2**, 532 (2003).
24. P. L. Gai, *Microsc. Microanal.* **8**, 21 (2002).
25. K. L. Liu *et al*., *Lab Chip* **8**, 1915 (2008).
26. N. de Jonge, D. B. Peckys, G. J. Kremers, D. W. Piston, *Proc. Natl. Acad. Sci. U.S.A.* **106**, 2159 (2009).
27. Materials and methods are available as supporting material on *Science* Online.
28. F. M. Ross, J. Tersoff, R. M. Tromp, *Phys. Rev. Lett.* **80**, 984 (1998).
29. J. E. Burke, D. Turnbull, in *Progress in Metal Physics*, vol. 3 (Pergamon Press, London, 1952), pp. 220–292.
30. The authors would like to thank A. Minor and J. Turner for their help with the initial tests on the liquid cells. This project is supported by the Director, Office of Science, Office of Basic Energy Sciences, Materials Sciences and Engineering Division of the U.S. Department of Energy under contract DE-AC02-05CH11231.

Supporting Online Material

www.sciencemag.org/cgi/content/full/324/5932/1309/DC1
Materials and Methods
Figs. S1 to S3
Movies S1 and S2
References

10 February 2009; accepted 8 April 2009
10.1126/science.1172104

Large-Area Synthesis of High-Quality and Uniform Graphene Films on Copper Foils

Xuesong Li,[1] Weiwei Cai,[1] Jinho An,[1] Seyoung Kim,[2] Junghyo Nah,[2] Dongxing Yang,[1] Richard Piner,[1] Aruna Velamakanni,[1] Inhwa Jung,[1] Emanuel Tutuc,[2] Sanjay K. Banerjee,[2] Luigi Colombo,[3]* Rodney S. Ruoff[1]*

Graphene has been attracting great interest because of its distinctive band structure and physical properties. Today, graphene is limited to small sizes because it is produced mostly by exfoliating graphite. We grew large-area graphene films of the order of centimeters on copper substrates by chemical vapor deposition using methane. The films are predominantly single-layer graphene, with a small percentage (less than 5%) of the area having few layers, and are continuous across copper surface steps and grain boundaries. The low solubility of carbon in copper appears to help make this growth process self-limiting. We also developed graphene film transfer processes to arbitrary substrates, and dual-gated field-effect transistors fabricated on silicon/silicon dioxide substrates showed electron mobilities as high as 4050 square centimeters per volt per second at room temperature.

Graphene, a monolayer of sp^2-bonded carbon atoms, is a quasi–two-dimensional (2D) material. Graphene has been attracting great interest because of its distinctive band structure and physical properties (*1*). Today, the size of graphene films produced is limited to small sizes (usually <1000 μm^2) because the films are produced mostly by exfoliating graphite, which is not a scalable technique. Graphene has also been synthesized by the desorption of Si from SiC single-crystal surfaces, which yields a multilayered graphene structure that behaves like graphene (*2*, *3*), and by a surface precipitation process of carbon in some transition metals (*4*–*8*).

Electronic application will require high-quality large-area graphene that can be manipulated to make complex devices and integrated in silicon device flows. Field-effect transistors (FETs) fabricated with exfoliated graphite have shown promising electrical properties (*9*, *10*), but these devices will not meet the silicon device scaling requirements, especially those for power reduction and performance. One device that could meet the silicon roadmap requirements beyond the 15-nm node was proposed by S. K. Banerjee *et al*. (*11*). The device is a "BisFET" (bilayer pseudospin FET) that is made up of two graphene layers separated by a thin dielectric. The ability to create this device can be facilitated by the availability of large-area graphene. Making a transparent electrode, another promising application of graphene, also requires large films (*6*, *12*–*14*).

At this time, there is no pathway for the formation of a graphene layer that can be exfoliated from or transferred from the graphene synthesized on SiC, but there is a way to grow and transfer graphene grown on metal substrates (*5*–*7*). Although graphene has been grown on a number of metals, we still have the challenge of growing large-area graphene. For example, graphene grown on Ni seems to be limited by its small grain size, presence of multilayers at the grain boundaries, and the high solubility of carbon (*6*, *7*). We have developed a graphene chemical vapor deposition (CVD) growth process on copper foils (25 μm thick in our experiment). The films grow directly on the surface by a surface-catalyzed process, and the film is predominantly graphene with <5% of the area having two- and three-layer graphene flakes. Under our processing conditions, the two- and three-layer flakes do not grow larger with time. One of the major benefits of our process is that it can be used to grow graphene on 300-mm copper films on Si substrates (a standard process in Si technology). It is also well known that annealing of Cu can lead to very large grains.

As described in (*15*), we grew graphene on copper foils at temperatures up to 1000°C by CVD of carbon using a mixture of methane and hydrogen. Figure 1A shows a scanning electron microscopy (SEM) image of graphene on a copper substrate where the Cu grains are clearly visible. A higher-resolution image of graphene on Cu (Fig. 1B) shows the presence of Cu surface steps, graphene "wrinkles," and the presence of non-uniform dark flakes. The wrinkles associated with the thermal expansion coefficient difference between Cu and graphene are also found to cross Cu grain boundaries, indicating that the graphene film is continuous. The inset in Fig. 1B shows transmission electron microscopy (TEM) images of graphene and bilayer graphene. With the use of a process similar to that described in (*16*), the as-grown graphene can be easily transferred to alternative substrates, such as SiO_2/Si or glass (Fig. 1, C and D), for further evaluation and for various applications; a detailed transfer process is described (*15*). The process and method used to transfer graphene from Cu was the same for the SiO_2/Si substrate and the glass substrate. Al-

[1]Department of Mechanical Engineering and the Texas Materials Institute, 1 University Station C2200, The University of Texas at Austin, Austin, TX 78712–0292, USA. [2]Department of Electrical and Computer Engineering, Microelectronics Research Center, The University of Texas at Austin, Austin, TX 78758, USA. [3]Texas Instruments, Dallas, TX 75243, USA.

*To whom correspondence should be addressed. E-mail: colombo@ti.com (L.C.); r.ruoff@mail.utexas.edu (R.S.R.)